

# Simulation of Deflection and Photon Emission of Ultra-Relativistic Electrons and Positrons in a Quasi-Mosaic Bent Silicon Crystal

Paulo E Ibañez-Almaguer<sup>1</sup>, Germán Rojas-Lorenzo<sup>1</sup>, Maykel Márquez-Mijares<sup>1</sup>, Jesús Rubayo-Soneira<sup>1</sup>, Gennady B Sushko<sup>2</sup>, Andrei V Korol<sup>2</sup>, and Andrey V Solov'yov<sup>2\*</sup>

E-mail: paulo.ibanez@instec.cu, solovyov@mbnresearch.com

<sup>1</sup> Instituto Superior de Tecnologías y Ciencias Aplicadas - Universidad de La Habana (InSTEC-UH), Ave. Salvador Allende 1110, 10400 La Habana, Cuba

<sup>2</sup> MBN Research Center, Altenhöferallee 3, 60438 Frankfurt am Main, Germany

**Abstract.** A comprehensive numerical investigation has been conducted on the angular distribution and spectrum of radiation emitted by 855 MeV electron and positron beams while traversing a ‘quasi-mosaic’ bent silicon (111) crystal. This interaction of charged particles with a bent crystal gives rise to various phenomena such as channeling, dechanneling, volume reflection, and volume capture. The crystal’s geometry, emittance of the collimated particle beams, as well as their alignment with respect to the crystal, have been taken into account as they are essential for an accurate quantitative description of the processes. The simulations have been performed using a specialized relativistic molecular dynamics module implemented in the MBN Explorer package. The angular distribution of the particles after traversing the crystal has been calculated for beams of different emittances as well as for different anticlastic curvatures of the bent crystals. For the electron beam, the angular distributions of the deflected particles and the spectrum of radiation obtained in the simulations are compared with the experimental data collected at the Mainz Microtron facility. For the positron beam such calculations have been performed for the first time. We predict significant differences in the angular distributions and the radiation spectra for positrons versus electrons.

*Keywords:* channeling, ‘quasi-mosaic’ bent crystal, collimated particle beams

Submitted to: *J. Phys. B: At. Mol. Opt. Phys.*

## 1. Introduction

The interaction of high-energy charged particles with bent crystals significantly depends on the relative orientation of the beam and the target. In a crystal, the positions of

\*Corresponding author.

constituent atoms follow certain regular pattern, thus forming an ordered structure of the crystalline environment. As a result, the crystal atoms can be viewed as been arranged in strings or/planes. Lindhard has demonstrated [1] that this arrangement of atoms produces an electrostatic field that affects charged particles passing through a crystal at small angles with respect to crystallographic planes (or axes) resulting in a specific channeling motion when a particle moves along a plane experiencing correlated interactions with the atoms.

The study of the passage of ultra-relativistic charged particle beams through oriented crystals (including the phenomenon of channeling) has emerged as a wide-ranging field of research [2–5]. Various applications have been suggested including beam steering [6–8], collimation [9], focusing [10], and extraction [2]. Theoretical and experimental investigations of channeling and other related phenomena have generated valuable knowledge [11–16]. Over the last decade, a series of experiments has been conducted at various accelerator facilities with the objective of examining channeling and radiation emission in bent crystals [6, 8, 17].

In this manuscript we present an independent analysis of the passage of 855 MeV electrons and positrons through an oriented bent silicon crystal and of the radiation emitted by the particles. The analysis is based on the results of calculations carried out within the framework of relativistic classical molecular dynamics by means of the MBN Explorer software package [18–20] and a supplementary special multitask software toolkit MBN Studio [21]. The purpose of the package is to serve as a versatile computer program enabling the study of molecular systems of different origin encompassing spatial scales ranging from the atomic level to the mesoscopic domain. The results obtained in the current simulations include angular distributions of the particles after passing through the crystal target and the spectral distribution of the radiation. In the case of electrons, our results are compared to the experimental data presented in Ref. [6] for the angular distributions and in Ref. [17] for the emission spectra.

The experiments [6, 17] were performed at the MAInzer MIcrotron (MAMI) facility with a highly collimated 855 MeV electron beam. The beam was incident on a ultra-thin silicon bent crystal. Bending of the (111) planes was due to the ‘quasi-mosaic’ effect [22–24] that appeared as a result of the primary deformation created by a specially designed holder [25]. After passing through the target, the electrons were deflected by magnets and thus separated from the emitted photons. This enabled measurement of both the angular distribution of the deflected electrons and the spectra of the emitted radiation.

Recently, it has been demonstrated [13] that accounting for specific geometry of a ‘quasi-mosaic’ bent crystal (qmBC) and its orientation with respect to the incident beam as well as for the beam’s transverse size and emittance is essential for an accurate quantitative description of experimental results on the beam deflection by such crystals. In the current simulations, these parameters have been accounted for along with the crystal thickness and curvature radii. The simulations have been performed for both electron and positron beams with similar characteristics. The predictions made for the

positrons are highly relevant to the experiments with the positron test beam which is planned to be constructed at MAMI within the framework of the ongoing European project TECHNO-CLS [26]. This project aims at the breakthrough in technologies require for the practical realisation of novel crystal-based gamma-ray Light Sources that can be constructed through exposure of oriented crystals to the beams of ultra-relativistic charged particles [5, 27].

This contribution is organized as follows: In the next section, we outline the methodology utilized in the simulations as well as the parameters of the crystal target and its alignment with respect to the beam following the description of the experimental setup [6, 17]. The outcomes of the calculations are analyzed in Results and Discussion section, and a summary of the results obtained is given in Conclusions.

## 2. Methodology

In this paper we employ the method of relativistic classical molecular dynamics [28], which is implemented in the MBN Explorer package, to simulate the motion of ultra-relativistic charged particles within the electrostatic field of a crystalline medium. This approach involves generating a significant number  $N$  of statistically independent trajectories for projectile particles. These trajectories can then be further analyzed to provide a quantitative characterization of the particles' motion and the radiation they emit.

To model the motion of an ultra-relativistic particle with mass  $m$ , charge  $q$ , and energy  $\epsilon$  in a medium, the following relativistic equations of motion are integrated:

$$\begin{cases} \dot{\vec{r}} = \vec{v} \\ \dot{\vec{p}} = q\vec{E} \end{cases} . \quad (1)$$

The instantaneous position and velocity of the particle are  $\vec{r} = \vec{r}(t)$  and  $\vec{v} = \vec{v}(t)$  respectively. A dot above the letter denotes differentiation with respect to time  $t$ . The momentum  $\vec{p}$  in terms of velocity reads  $\vec{p} = m\gamma\vec{v}(t)$  where  $\gamma = \epsilon/mc^2$  stands for the relativistic factor, where  $c$  is the speed of light in vacuum.

The electric field in the point  $\vec{r}$  is calculated as  $\vec{E}(\vec{r}) = -\nabla_{\vec{r}}\phi(\vec{r})$  with  $\phi(\vec{r})$  standing for the field's potential. This quantity is calculated as the sum of potentials of individual atoms, which contribution is not negligible. The atomic potentials can be computed within the frameworks of the approximations due to Molière [29] and Pacios [30].

To ensure that all trajectories are statistically independent and each one corresponds to a unique crystalline environment, the positions of the atoms are generated accounting for random displacement from the nodes due to thermal vibrations. In addition to this, initial transverse coordinates and velocities are generated randomly, with their distribution determined by the transverse size and divergence of the beam.

Silicon crystal has the diamond cubic structure and thus its mechanical properties are highly anisotropic. As a result, when the crystalline medium is subjected to two moments of force to achieve primary curvature, some secondary curvatures may arise

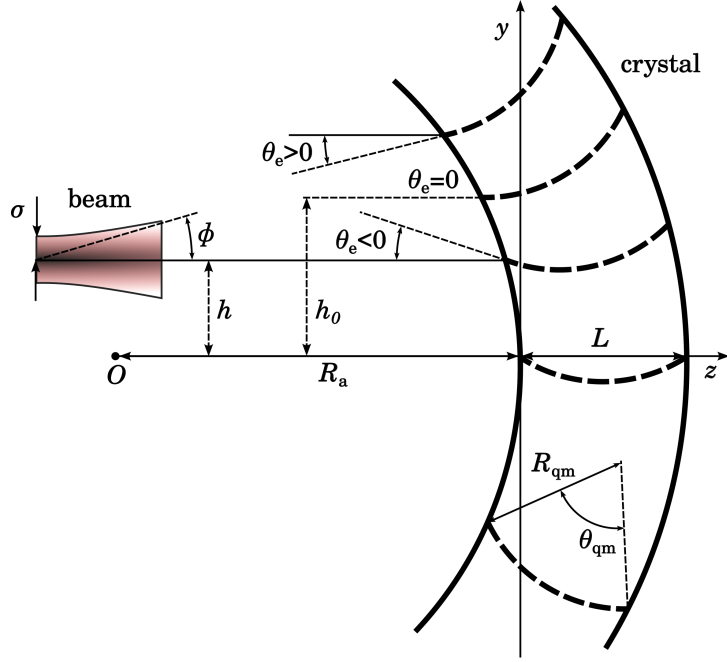


**Figure 1.** Geometry of a ‘quasi-mosaic’ bent crystal plate of a thickness  $L$  and its alignment with respect to an incident beam of a transverse size  $\sigma$  and angular divergence  $\phi$ . The point  $O$  denotes the center of anticlastic curvature of radius  $R_a$ . The Si(111) planes (thick dashed curves) are bent due to the QM effect with the curvature radius  $R_{qm}$ ;  $\theta_{qm} = L/R_{qm}$  stands for the QM bending angle. Other notations are explained in the text.

within the solid. A well-known secondary deformation results in the anticlastic curvature that occurs in the perpendicular direction with respect to the primary curvature. When the two curvatures are combined, the deformed crystal acquires the shape of a saddle. Another type of the deformation caused by anisotropic effects is the ‘quasi-mosaic’ (QM) curvature [22]. The qmBCs belong to a class of bent crystals featuring two curvatures of two orthogonal crystallographic planes. In the silicon crystals used in the experiment [6, 17] the (111) planes were bent due to the QM effect.

Following Ref. [13], Fig. 1 illustrates the alignment of a qmBC and an incident beam. It is important to note that the representation is merely a schematic and not to scale. The anticlastic radius  $R_a$  is on the order of meters, and the QM radius  $R_{qm}$  is on the order of centimeters, while the thickness  $L$  is on the order of tens of micrometers. Therefore, the actual curvatures are not as pronounced as they are shown in the figure.

In the coordinate system chosen, the  $z$ -axis is aligned with the incident beam direction which is normal to the face of the not deformed (i.e., not bent) crystal plate. The primary curvature (not shown in the figure) causes the plate to bend around the  $y$  direction towards the positive direction of the  $z$ -axis. The anticlastic curvature of radius  $R_a$  bends the plate around the  $x$  direction towards the negative  $z$ -axis. In Fig. 1 the point  $O$  denotes the center of anticlastic curvature. The QM bending of the (111) crystallographic planes is around the  $x$  direction ( $R_{qm}$  denotes the QM bending radius).

In the present paper the case of a planar channeling is considered. Therefore, in the simulations, the  $z$ -axis direction has been chosen well away from major crystallographic axes to avoid axial channeling.

The entrance angle  $\theta_e$  between the incident beam direction and the nearest QM bent plane at the entry of the crystal depends on the  $y$ -coordinate  $h$  of the center of the beam,  $\theta_e(h) = (h - h_0)/R_{qm}$ . The quantity  $h_0 = \theta_{qm}R_a/2$  stands for the displacement at which the entrance angle is zero. A probability of a particle to be accepted into the channeling mode at the crystal entrance becomes significant if  $\theta_e$  does not exceed Lindhard's critical angle  $\theta_L$ . For an ideally collimated beam ( $\phi = 0$ ) this condition is met for the particles that enter the crystal within the interval  $h_0 \pm \theta_L R_a$ . The projectiles that are accepted at  $y = h$  and channel through the whole crystal are deflected by the angle lying within the interval  $\theta_e(h) + \theta_{qm} \pm \theta_L$  [13].

The particles entering the crystal in the region  $-h_0 < h < h_0$  (i.e. with  $\theta_e > 0$ ) can experience either volume capture [31] or volume reflection [32] of the curved crystalline planes during their propagation through the crystal volume. These events take place at the points at which a particle's trajectory becomes tangent to the planes. For a given value of  $h$  the point of the volume capture and the volume reflection is positioned at the distance  $L/2 - R_{qm}h/R_a$  from the entrance point to the crystal. This distance is equal to zero if  $h = h_0$  and to  $L$  for  $h = -h_0$ . Particles that move in the channeling regime after the volume capture exit the crystal at the angle  $\theta_s = \theta_e(h) + \theta_{qm}/2 + h/R_a$ . In the event of volume reflection particles are deflected by some characteristic angle  $\theta_{vr}$  which does not depend on the choice of  $h$  but is determined by radius  $R_{qm}$  and the particle energy. After the volume reflection particles experience multiple scattering within the remaining crystal volume and exit the crystal at the characteristic angle  $\theta_{vr}$ .

If at the entrance  $h > h_0 + \theta_L R_a$  then the particle is neither accepted nor volume reflected but experiences multiple scattering which becomes closer to the scattering in the amorphous medium as  $h$  increases.

To reproduce the geometry shown in Fig. 1 with the MBN Explorer and MBN Studio packages, the first step is to generate a non-deformed crystalline medium within the spatial region from  $z = 0$  to  $z = L$  [28]. Then, two transformations can be applied to the silicon crystal structure: (i) 'quasi-mosaic' bending of the Si(111) planes, and (ii) anticlasic bending of the planes parallel to the  $xy$ -plane [13]. Since the crystal has a finite thickness, the equations of motion Eq. 1 can be integrated from some point  $z = -\Delta z$  before the entrance to the crystal up to  $z = L + \Delta z$  which is beyond the exit point  $z = L$ . Doing this, one accounts for the particle-crystal-atoms interaction as it approaches the crystal, passes through it and moves away from the crystal. Typically, the value of  $\Delta z$  equals to the cutoff radius  $\rho_{max}$  for the potential chosen to describe the particle-atom interaction. This potential decreases rapidly with increasing distance from the atom. Therefore, when calculating the potential acting on the particle in the crystal or in its vicinity, one can account only for those atoms that are located inside a sphere of the radius  $\rho_{max}$  with the center at the instant position of the particle.

The simulation parameters have been selected according to the experiment [17]:

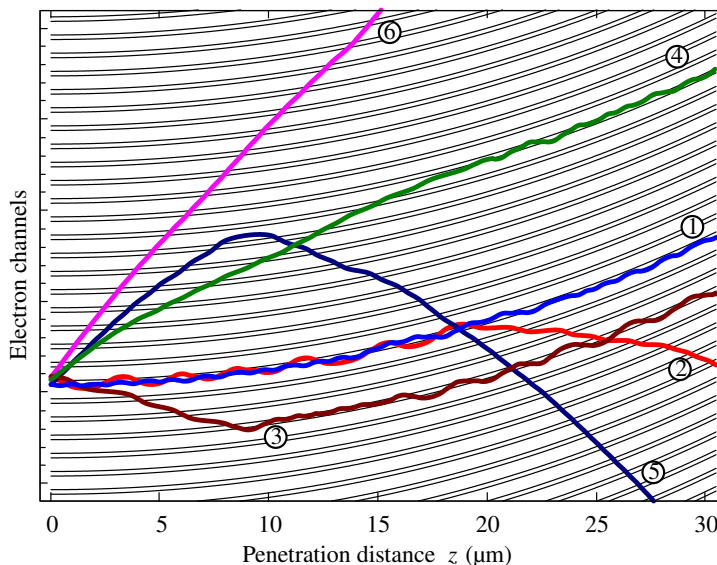


**Figure 2.** Selected trajectories showcasing processes associated with the interaction of electrons with a bent crystal. The thin lines represent the bent Si(111) planes and the thick lines represent the projection in the  $yz$ -plane of the simulated electron trajectories.

The crystal thickness is  $L = 30.5 \mu\text{m}$  and the QM bending radius  $R_{\text{qm}} = 3.35 \text{ cm}$ . The anticlasic radius was not specified in the cited paper. Basing on the value  $R_a = 3.66 \text{ m}$  obtained in the experimental measurements [23] of the quasi-mosaic crystals bent with smaller QM radii ( $R_{\text{qm}} \approx 1.5 - 1.8 \text{ cm}$ ), in the current simulations two anticlasic radii  $R_a = 5$  and  $10 \text{ m}$  have been considered.

The simulations have been carried out for 855 MeV Gaussian beams of the transverse size  $\sigma = 50 \mu\text{m}$  and of two divergences  $\phi = 10$  and  $20 \mu\text{rad}$ . The passage of the particles has been simulated for the following two different beam–crystal geometries (see Fig. 1): (i)  $y = h_0$  which corresponds to beam alignment with bent Si(111) planes at the entrance ( $\theta_e = 0$ ), (ii)  $y = h < h_0$  with  $h$  corresponding to the entrance angle  $\theta_e = -10 \mu\text{rad}$ .

Sets of statistically independent trajectories have been calculated once the geometry and the beam characteristics were defined. Figure 2 displays several simulated trajectories selected to represent processes related to the interaction of an electron beam with the crystal. Thin lines show the  $(y, z)$  cross sections of the bent Si(111) planes separated with alternate wide ( $d_W = 2.352 \text{ \AA}$ ) and short ( $d_S = 0.784 \text{ \AA}$ ) spacings. The electron channels of the width  $d = d_W + d_S = 3.136 \text{ \AA}$  are defined as the regions between the centerlines of the two nearest wide spacings. Tick marks shown on the left vertical axis of the figure mark the channels' boundaries at the crystal entrance.

When the entrance angle is smaller than Lindhard's critical angle  $\Theta_L$  (maximum incident angle consistent with the channeling condition [1]) particles may be accepted into a channel. Within the continuous potential approximation one writes  $\Theta_L = (2U_0/\epsilon)^{1/2}$  with  $U_0$  standing for the depth of the continuous interplanar potential.

Using the value  $U_0 \approx 24$  eV for the Si(111) channel (see, e.g., Ref. [33]) one calculates  $\Theta_L \approx 0.24$  mrad for a 855 MeV projectile. An accepted particle can traverse the entire crystal in the channeling mode (channeling: trajectory 1), or it may exit the channel at some point in the crystal bulk (dechanneling: trajectory 2). A non-accepted particle starts its motion in the over-barrier mode but can be captured into the channeling mode afterwards (rechanneling: trajectory 3).

When the incident angle of a particle is greater than  $\Theta_L$  it starts to move in the over-barrier mode. Due to the crystal bending, at some point inside the crystal particle's velocity may become tangent to the crystal plane resulting in the particle's capture into the channeling mode (volume capture: trajectory 4). Another scenario for an over-barrier particle, which moves under a small angle to the bent crystal, implies a reflection to the side opposite the bend (volume reflection [32]: trajectory 5). Finally, a non-accepted particle can pass through the whole crystal in the over-barrier mode (trajectory 6).

The simulated trajectories, being statistically independent, can be used to calculate spectral and angular distributions of the emitted radiation. The averaged spectral distribution of energy emitted within the cone  $\theta \leq \theta_0$  with respect to the incident beam is computed as follows:

$$\left\langle \frac{dE(\theta \leq \theta_0)}{d\omega} \right\rangle = \frac{1}{N} \sum_{n=1}^N \int_0^{2\pi} d\phi \int_0^{\theta_0} \theta d\theta \frac{d^3 E_n}{d\omega d\Omega}. \quad (2)$$

Here,  $\omega$  stands for the frequency of radiation,  $\Omega$  is the solid angle corresponding to the emission polar angles  $\theta$  and  $\phi$ , and  $d^3 E_n/d\omega d\Omega$  is the spectral-angular distribution of radiation emitted by a projectile moving along the  $n$ th trajectory,  $N$  stands for the total number of simulated trajectories. The numerical procedures implemented in MBN Explorer package to calculate these distributions [28] are based on the quasi-classical formalism due to Baier and Katkov [34]. This method combines classical description of the motion in an external field with the quantum corrections due to the radiative recoil.

The resulting spectrum accounts for channeling radiation owing to the motion of particles in the channeling mode, coherent and incoherent bremsstrahlung due to over-barrier motion, and the synchrotron-type radiation as result of the circular motion along an arc in a bent crystal.

### 3. Results and Discussion

#### 3.1. Angular distribution of electrons

The trajectories have been simulated utilizing atomic potentials derived from the Molière and the Pacios models for the electron-atom interaction. The results obtained for the angular distribution of the deflected electrons after interaction with the crystal turned out to be similar for both potentials. For the spectral distribution of the radiation it has been found that the calculations with the Pacios potential exhibit better agreement

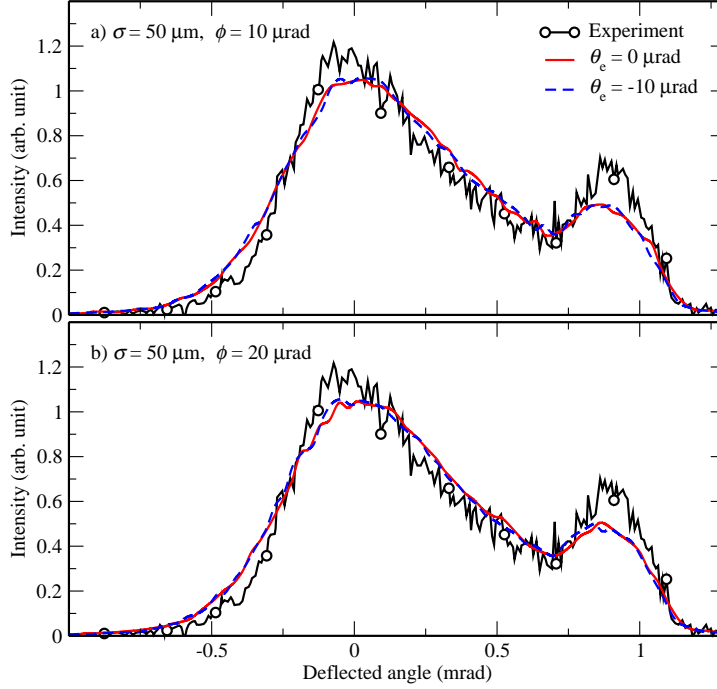


**Figure 3.** Angular distributions of deflected electrons. The simulations (lines without symbols) refer to a 855 MeV beam of the transverse size  $\sigma = 50 \mu\text{m}$  and angular divergences of  $\phi = 10 \mu\text{rad}$  (panel a) and  $\phi = 20 \mu\text{rad}$  (panel b) incident on a quasisaiaic Si(111) crystal with anticlassic radius  $R_a = 5 \text{ m}$ . Solid lines correspond to the distribution calculated for the entrance angle  $\theta_e = 0$ , dashed lines correspond to  $\theta_e = -10 \mu\text{rad}$ . The lines with circles stand for the experimental data reported in Ref. [6]. All dependencies are normalized to the unit area.

with the experimental results. This feature is in line with the analysis carried out earlier in Ref. [12].

The angular distributions calculated for the bent crystal with the anticlassic radius  $R_a = 5 \text{ m}$  are shown in Fig. 3. The simulate data refer to two entrance angles (see Fig. 1):  $\theta_e = 0$  (solid lines without symbols) and  $\theta_e = -10 \text{ mrad}$  (dashed lines). Two panels present the distributions simulated for different values of the beam divergence:  $\phi = 10 \mu\text{rad}$  (panel a) and  $\phi = 20 \mu\text{rad}$  (panel b). In both cases the beam size is fixed at  $\sigma = 50 \mu\text{m}$ . The experimental data shown were obtained by digitizing the graphical data presented for the channeling alignment in Figure 3 from Ref. [6].

The simulated and measured angular distributions have the characteristic pattern of two well pronounced peaks interlinked by an intermediate region. The peak on left side is primarily contributed by the electrons moving in the over-barrier mode from the entrance point up to the crystal exit. These particles experience multiple scattering from the crystal atoms which leads to the broadening of the angular distribution at the exit as compare to the angular divergence of the incident beam.

The main contribution to the right-side peak, which is centered at the QM bending angle  $\theta_{\text{qm}} = L/R_{\text{qm}} = 0.91 \text{ mrad}$  (see Fig. 1), is due to the electrons that channel through the entire crystal length. Additionally, electrons that are trapped in the



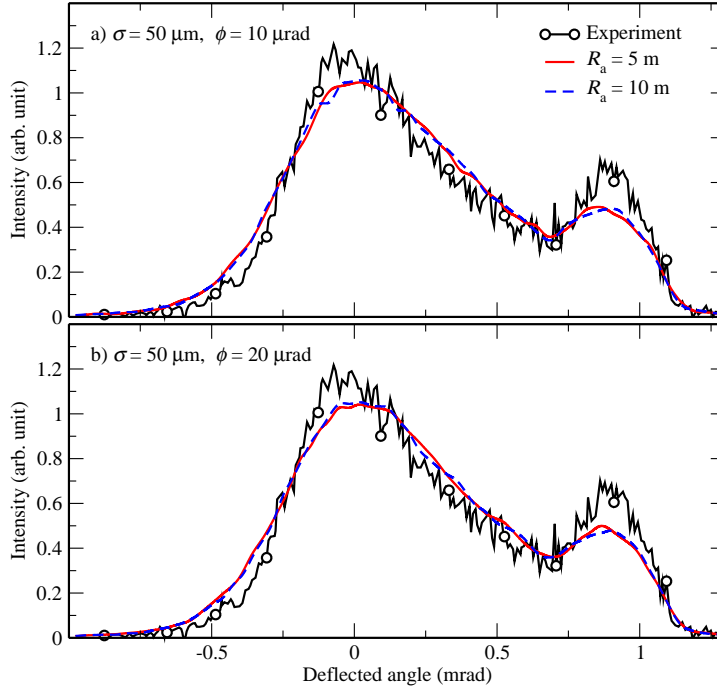


**Figure 4.** Angular distribution of the deflected electrons simulated for different values of the beam divergence ( $\phi = 10$  and  $20 \mu\text{rad}$  in the top and bottom graphs, correspondingly) and for two values of the anticlastic curvature radii  $R_a$  as indicated in the common legend shown in the top graph. All dependencies shown correspond to the beam transverse size  $\sigma = 50 \mu\text{m}$  and to the incident angle  $\theta_e = 0$ . Solid line with open circles corresponds to the experimental data reported in Ref. [6]. All distributions are normalized to the unit area.

channeling mode somewhere inside the crystal contribute to the distribution in the vicinity of this peak. The intermediate region is predominantly formed by electrons that are accepted in the channeling mode at the entrance but then dechannel at some point in the bulk.

Figure 3 shows that there are no significant differences between the distributions obtained for the two entrance angles  $\theta_e$ . In both cases, the peak values are smaller than the experimentally measured ones. This is because the simulation shows higher contribution from the dechanneling process compared to the experiment. Consequently, more electrons are deflected in the intermediate region resulting in the decrease in peak values and causing the peaks to shift towards each other.

The angular distributions of deflected electrons simulated for two values of the anticlastic curvature radius,  $R_a = 5$  and  $10 \text{ m}$ , are compared in Fig. 4. The simulations refer to the beam of the size  $\sigma = 50 \mu\text{m}$  incident on the crystal at  $\theta_e = 0$ . The top graph corresponds to the beam divergence  $\phi = 10 \mu\text{rad}$ , the bottom graph – to  $\phi = 20 \mu\text{rad}$ . The experimental data taken from Ref. [6] are also shown.

The angular distributions obtained for the two values of anticlastic curvature radii are similar, suggesting that for large values of  $R_a$ , the fraction of deflected electrons at each angle is independent of this parameter. Comparing the distributions shown in the

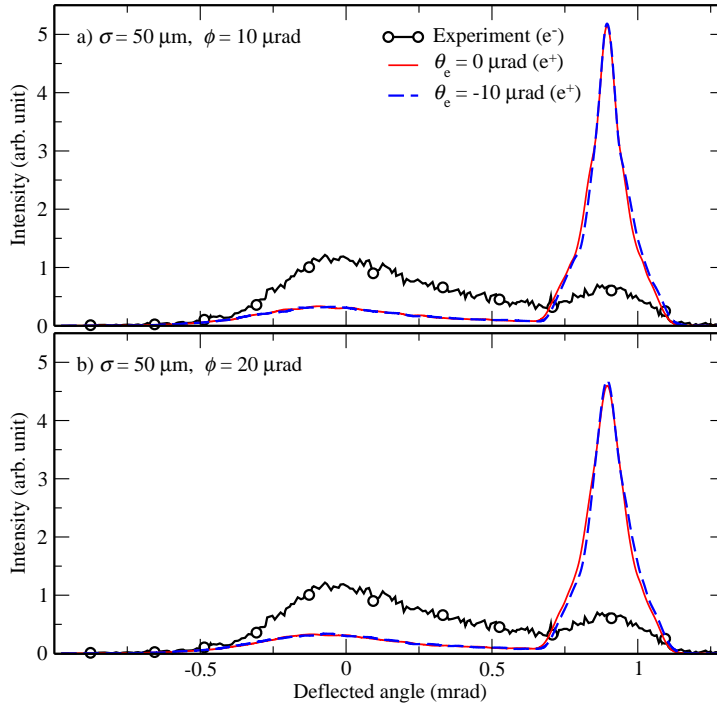


**Figure 5.** Similar as in Fig. 3 but for a 855 MeV positron beam incident on the quasi-mosaic Si(111) crystal. All simulated distributions refer to the anticlasic curvature radius  $R_a = 5$  m. The experimental data for electrons [6] are also shown.

top and bottom graphs, one concludes that they are weakly dependent on the beam divergence. This is understandable since the divergences considered are much smaller than Lindhard's critical angle  $\theta_L \approx 240 \mu\text{rad}$ .

### 3.2. Angular distribution of positrons

Angular distributions of positrons deflected by the same quasi-mosaic bent silicon crystal has also been analyzed. Figure 5 shows the distributions obtained in the simulations of the 855 MV positron beams with transverse size  $\sigma = 50 \mu\text{m}$  and divergences  $\phi = 10$  and  $20 \mu\text{rad}$  (top and bottom graphs, respectively) incident on the bent Si(111) crystal with the anticlasic curvature radius  $R_a = 5$  m. As in the case of electrons (see Fig. 3) two incident geometries have been considered corresponding to the entrance angles  $\theta_e = 0$  and  $-10$  mrad. The experimentally measured distribution of electrons [6] is also shown for the sake of comparison.

Most of the positrons pass through the whole crystal moving in the channeling mode. As a result, the channeling peak at  $\theta_{qm} = 0.91$  mrad is much more pronounced than in the electron distribution.

The positrons that are not accepted in the channeling regime at the entrance (as well as those that are accepted but dechannel shortly after) and propagate throughout the entire crystal in the over-barrier mode exhibit a behavior similar to that of the electrons. For positrons, the left peak is centered at a larger negative angle than the peak in the

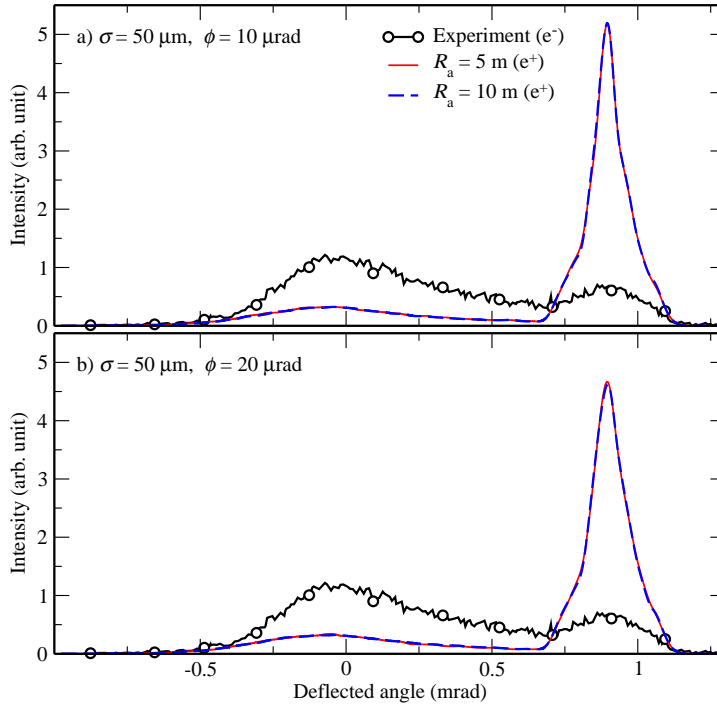


**Figure 6.** Similar as in Fig. 4 but for 855 MeV positron beams incident on the quasi-mosaic Si(111) crystal. The experimental data for electrons [6] are also shown.

electron distribution. This indicates that relative fraction of volume reflected positrons (which contribute to the distribution in the domain of negative deflection angles) is larger than that for electrons. The positron dechanneling rate is much less than the dechanneling rate of electrons of the same energy. Therefore, the channeling peak in the positron distribution is enhanced greatly whereas the left-peak value is notably smaller than in the electron distribution.

As in the case of electrons, the angular distributions of deflected positrons are similar for the two investigated entrance angles, see Fig. 5. However, for positrons, the impact of the beam divergence on the distribution is more pronounced. This is clearly seen if comparing the channeling peak values in the top and bottom graphs: for the beam with smaller divergence (top) the channeling peak is ca 10 % higher than for the wider beam (bottom).

Angular distributions simulated for the positron beams centered at a  $y = h_0$  (corresponding to tangential geometry at the crystal entrance, see Fig. 1) incident on Si(111) crystals with anticlastic radii  $R_a = 5$  and 10 m are shown in Fig. 6. Two values of the beam emittance have been considered while maintaining constant value of the beam's transverse size. The distribution measured in the experiment with electrons [6] is shown for comparison.

The results from this figure corroborate the fact that for large anticlastic radii, the angular distribution of charged particles becomes independent on it. Furthermore, for both radii, the channeling peak becomes less intensive and broader as the value of the

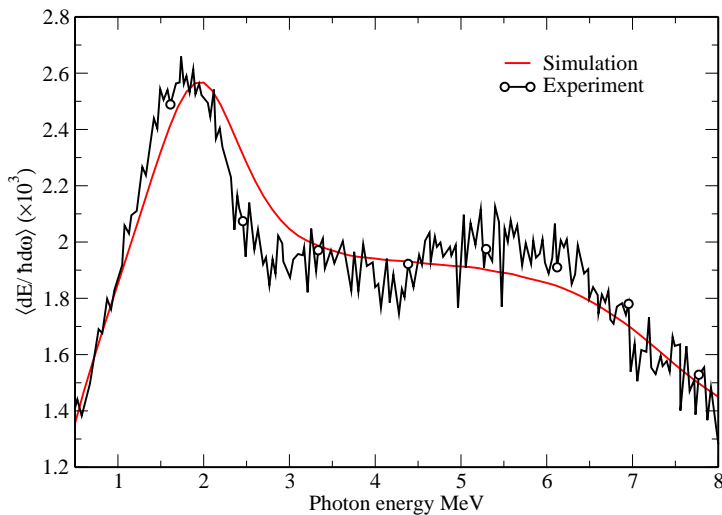


**Figure 7.** Spectral distribution of radiation emitted by 855 MeV electrons passing through the ‘quasi-mosaic’ bent Si(111) crystal. Solid (red) curve without symbols stands for the results of the current simulations; solid (black) curve with symbols corresponds to the experimental data reported in Ref. [17]. Note that the values of  $\langle dE/d(h\omega) \rangle$  are shown being multiplied by the factor  $10^3$ . The intensity of the of background radiation due to the incoherent bremsstrahlung is approximately  $0.35 \times 10^{-3}$ .

beam divergence increases.

The atomistic approach implemented in MBN Explorer allows one to look for and to identify various processes mentioned earlier (see Fig. 2) for each simulated trajectory. This enables a more detailed analysis of the contribution of these processes to the overall distribution.

### 3.3. Spectra of emitted radiation

MBN Explorer allows one to calculate spectral and angular distributions of the radiation emitted by beam particles using the scheme presented by Eq. (2). For each simulated trajectory (the index  $n = 1, 2, \dots, N$  enumerates the trajectories) the spectral-angular distributions  $d^3E/d\omega d\Omega$  are calculated for specified values of the emitted photon energy  $\hbar\omega$  and emission angle  $\theta$  (by default, the full range from 0 to  $2\pi$  is assumed for the polar angle  $\varphi$ ). Integrating numerically the individual spectral-angular distributions over  $\theta$  within a specified cone  $\theta_0$  with respect to the incident beam and carrying out averaging over all trajectories one calculates averaged spectral distribution  $\langle dE/d(\hbar\omega) \rangle$  of radiation emitted by the beam.

In this section, the distributions  $\langle dE/d(\hbar\omega) \rangle$  presented have been calculated for 855 MeV electron and positron beams incident on the bent Si crystal being aligned with the (111) at the entrance (i.e.,  $\theta_e = 0$ ). The data refer to the anticlasic curvature radius  $R_a = 5$  m, and to the beam transverse size  $\sigma = 50 \mu\text{m}$  and divergence  $\phi = 20 \mu\text{rad}$ . These values of  $\sigma$  and  $\phi$  correspond to the emittance  $\sigma \times \phi$  of the electron beam

used in the experiment [17] where the spectral distribution of the emitted radiation was measured. The calculated spectra presented below correspond to the emission cone  $\theta_0$  equal to  $\theta_{qm} + 3/\gamma \approx 2.7$  mrad. This cone is wide enough to collect almost all emission radiated from each simulated trajectory. Its value is slightly larger than the cone  $\theta_0 \approx 2.4$  mrad use in the experiment.

Figure 7 presents the calculated spectral distribution of radiation (red solid line without symbols) emitted by the electron beam and the experimentally measured spectrum (black solid line with open circles) [17]. The experimental values has been obtained by digitalizing the "CR-exp" curve in figure 2 in the cited paper. The experimental data were reported in arbitrary units, whereas the current simulations produce absolute values. Therefore, to carry out the comparison both results the experimental data has been re-scaled to produce the same area as in the simulations.

By comparing the curves in Fig. 7 one can conclude that there is a good agreement between the experimental and theoretical results both in terms of the spectral distribution shape and absolute values. In the photon energy interval presented,  $\hbar\omega = 0.5 - 8$  MeV, the spectrum is dominated by the radiation produced by the channeling electrons, i.e. by the channeling radiation (ChR). The peak value of ChR at about 1.8 MeV is approximately 7 times larger than the intensity of the incoherent bremsstrahlung background (not shown in the figure).

The spectrum of radiation emitted by the positron is shown in Fig. 8. In the photon energy interval  $\hbar\omega \approx 1 - 2$  MeV the spectrum is dominated by the peak of ChR, which is more powerful and narrower than in the electron case. The profile of the peak is similar to the profile of the emission into the fundamental harmonic in a planar undulator, in which an ultra-relativistic charge moves along harmonic trajectory (see, e.g., [4] and references therein). It is not surprising, since the channeling oscillations of positrons are nearly harmonic (see, e.g., examples of simulated positron trajectories presented in Refs. [11, 35]). The second peak at  $\hbar\omega \lesssim 4$  MeV, although much less intensive and much broader, corresponds to the emission into the second harmonic of ChR. Channeling oscillations of electrons are strongly anharmonic. As a result, their ChR is spread over broader interval of the photon energies making the spectral distribution less similar to that intrinsic to the undulator radiation.

The feature that is clearly seen in the positron emission spectrum is due to a circular motion of the channeling particles. This motion leads to the emission of a synchrotron-type radiation (SR), which contributes to the low-energy part of the spectrum,  $\hbar\omega \lesssim 0.2$  MeV. This feature, predicted theoretically in Ref. [36], has been recently analysed quantitatively by means of relativistic molecular dynamics simulations [33, 35, 37]. The characteristic energy  $\hbar\omega_c$  (in MeV) beyond which intensity of SR decreases rapidly [38] can be written as follows:  $\hbar\omega_c \approx 0.22\epsilon^3/R$  with  $\epsilon$  in GeV and the curvature radius  $R$  in cm. For a 855 MeV projectile and for  $R = R_{qm} = 3.35$  cm this estimate produces  $\hbar\omega_c \approx 50$  keV.

We note that the mechanism of the SR emission by a channeling particle does not depend on the sign of its charge. However, as a rule the dechanneling length for

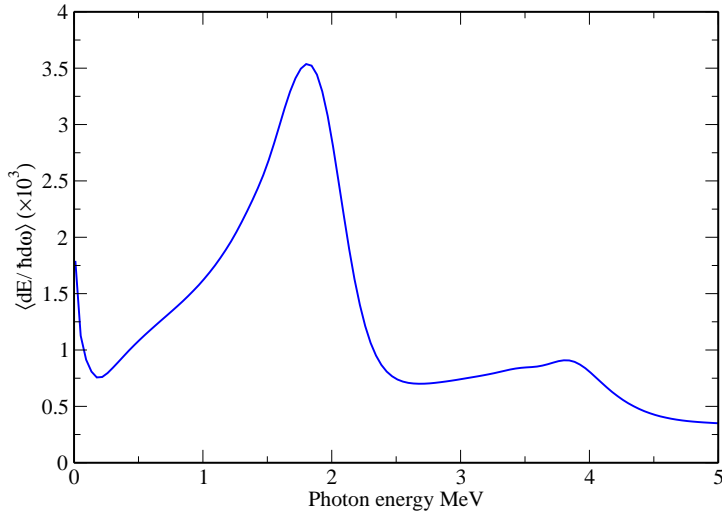


**Figure 8.** Spectral distribution of radiation emitted by 855 MeV positrons passing through the ‘quasi-mosaic’ bent Si(111) crystal. Note that the values of  $\langle dE/d(h\omega) \rangle$  are shown being multiplied by the factor  $10^3$ .

a positron is much larger than for an electron of the same energy, therefore, the SR emitted by a channeling positron is more intensive as it can experience circular motions over larger distances channels. In the electron emission spectrum, Fig. 7, the increase in the low-energy part of the spectrum is not seen because its starts below the lowest photon energy of 0.5 MeV shown in the figure. This cut-off has been introduced to match the interval of photon energies investigate in the experiment [17].

#### 4. Conclusion

The atomistic approach of the MBN Explorer allows one to monitor the changes in the distribution of electrons and positrons deflected by a  $30.5 \mu\text{m}$  thick quasi-mosaic bent Silicon crystal upon the parameters of the beam and the crystal bending, as well as to obtain the spectrum of emitted radiation.

The simulation results for the 855 MeV electron beams of different emittances and orientations with respect to the crystal have been compared with experimental data. A good agreement of the simulations with the experiment can be stated. Some discrepancies have been noted in the angular distribution of deflected electrons. Possible reasons for the discrepancies can be attributed to the particular force fields (Molière and Pacios ) chosen to describe the particle-atom interaction in the course of simulations, and to the phenomena not accounted for (e.g., quantum effects in multiple scattering in crystals [39, 40]). The spectral distribution of the radiation emitted by the electron beam is in good agreement with the experimentally measured spectrum.

Similar sets of simulations have been carried out for the positron beam of the same energy, transverse size and divergence. The predictions have been made on the angular distributions of the deflected positrons as well as on the spectral distribution of the

emitted radiation. A comparison of the results of simulations for electrons and positrons has been carried out. These results are of interest in connection to the experiments planned to be carried out at the MAMI facility upon finishing the construction of the test positron beam (provisionally scheduled for the year 2024). This activity is carried out within the ongoing project [26].

### *Acknowledgements*

We acknowledge support by the European Commission through the N-LIGHT Project within the H2020-MSCA-RISE-2019 call (GA 872196) and the EIC Pathfinder Project TECHNO-CLS (Project No. 101046458). PEIA, GRL, MMM and JRS would like to thank NA223LH-INSTEC-003 project from InSTEC-UH. We also acknowledge the Frankfurt Center for Scientific Computing for providing computer facilities.

### *Authors contributions*

All authors were involved in the preparation of the manuscript and contributed equally to this work. All authors have read and approved the final manuscript.

### *Data Availability Statement*

This manuscript has no associated data or the data will not be deposited. [Authors' comment: All data generated are included into this published article. Data will be made available on request.].

### *Conflict of interest*

The authors declare no conflict of interest.

## References

- [1] Lindhard J 1965 *Kongel. Dan. Vidensk. Selsk., Mat.-Fys. Medd.* **34** URL <https://www.osti.gov/biblio/4536390>
- [2] Biryukov V M, Chesnokov Y A and Kotov V I 1997 *Crystal Channeling and Its Application at High-Energy Accelerators* 1st ed (Berlin: Springer Berlin, Heidelberg) ISBN 978-3-540-60769-4
- [3] Uggerhøj U I 2005 *Rev. Mod. Phys.* **77**(4) 1131–1171
- [4] Korol A V, Solov'yov A V and Greiner W 2014 *Channeling and Radiation in Periodically Bent Crystals* 2nd ed (Berlin, Heidelberg: Springer-Verlag)
- [5] Korol A V and Solov'yov A V 2022 *Novel Light Sources beyond Free Electron Lasers* (Cham: Springer Nature Switzerland AG)
- [6] Mazzolari A, Bagli E, Bandiera L, Guidi V, Backe H, Lauth W, Tikhomirov V, Berra A, Lietti D, Prest M, Vallazza E and De Salvador D 2014 *Phys. Rev. Lett.* **112**(13) 135503
- [7] Mazzolari A, Romagnoni M, Camattari R, Bagli E, Bandiera L, Germogli G, Guidi V and Cavoto G 2018 *Eur. Phys. J. C* **78** 720
- [8] Wienands U, Markiewicz T W, Nelson J, Noble R J, Turner J L, Uggerhøj U I, Wistisen T N, Bagli E, Bandiera L, Germogli G, Guidi V, Mazzolari A, Holtzapple R and Miller M 2015 *Phys. Rev. Lett.* **114**(7) 074801

- [9] Scandale W, Arduini G, Assmann R, Bracco C, Gilardoni S, Ippolito V, Laface E, Losito R, Masi A, Metral E, Previtali V, Redaelli S, Silari M, Tlustos L, Bagli E, Baricordi S, Dalpiaz P, Guidi V, Mazzolari A, Vincenzi D, Della Mea G, Lombardi A, De Salvador D, Vallazza E, Bolognini D, Hasan S, Lietti D, Mascagna V, Mattera A, Prest M, Cavoto G, Ludovici L, Mirarchi D, Santacesaria R, Valente P, Murtas F, Afonin A G, Chesnokov Y A, Maishev V A, Yazynin I A, Kovalenko A D, Taratin A M, Denisov A S, Gavrikov Y A, Ivanov Y M, Lapina L P, Malyarenko L G, Skorobogatov V V, Suvorov V M, Vavilov S A, Mokhov N, Still D, Robert-Demolaize G, Markiewicz T and Oriunno M 2010 *Phys. Lett. B* **692** 78–82
- [10] Scandale W, Arduini G, Cerutti F, Garattini M, Gilardoni S, Lechner A, Losito R, Masi A, Mirarchi D, Montesano S, Natochii A, Redaelli S, Rossi R, Smirnov G, Breton D, Burmistrov L, Chaumat V, Dubos S, Maalmi J, Puill V, Stocchi A, Bagli E, Bandiera L, Romagnoni M, Guidi V, Mazzolari A, Murtas F, Addesa F, Cavoto G, Iacoangeli F, Galluccio F, Afonin A G, Chesnokov Y A, Durum A A, Maishev V A, Sandomirskiy Y E, Yanovich A A, Kovalenko A D, Taratin A M, Denisov A S, Gavrikov Y A, Ivanov Y M, Lapina L P, Malyarenko L G, Skorobogatov V V, Auzinger G, Borg J, James T, Hall G and Pesaresi M 2019 *Nucl. Instrum. Methods Phys. Res., Sect. B* **446** 15–18
- [11] Korol A V, Sushko G B and Solov'yov A V 2021 *Eur. Phys. J. D* **75** 107
- [12] Haurylavets V V, Leukovich A, Sytov A, Bandiera L, Mazzolari A, Romagnoni M, Guidi V, Sushko G B, Korol A V and Solov'yov A V 2021 *Eur. Phys. J. Plus* **137** 34
- [13] Sushko G B, Korol A V and Solov'yov A V 2022 *Eur. Phys. J. D* **76** 236
- [14] Bandiera L, Bagli E, Guidi V, Mazzolari A, Berra A, Lietti D, Prest M, Vallazza E, De Salvador D and Tikhomirov V 2013 *Phys. Rev. Lett.* **111**(25) 255502
- [15] Sytov A I, Guidi V, Tikhomirov V V, Bagli E, Bandiera L, Germogli G and Mazzolari A 2016 *Eur. Phys. J. C* **76** 77
- [16] Wistisen T N, Uggerhøj U I, Wienands U, Markiewicz T W, Noble R J, Benson B C, Smith T, Bagli E, Bandiera L, Germogli G, Guidi V, Mazzolari A, Holtzapfel R and Tucker S 2016 *Phys. Rev. Accel. Beams* **19**(7) 071001
- [17] Bandiera L, Bagli E, Germogli G, Guidi V, Mazzolari A, Backe H, Lauth W, Berra A, Lietti D, Prest M, De Salvador D, Vallazza E and Tikhomirov V 2015 *Phys. Rev. Lett.* **115**(2) 025504–025509
- [18] Solov'yov I A, Yakubovich A V, Nikolaev P V, Volkovets I and Solov'yov A V 2012 *J. Comput. Chem.* **33** 2412–2439
- [19] Solov'yov I A, Korol A V and Solov'yov A V 2017 *Multiscale Modeling of Complex Molecular Structure and Dynamics with MBN Explorer* 1st ed (Cham: Springer) ISBN 978-3-319-56085-4
- [20] MBN Explorer and MBN Studio software URL <https://www.mbnresearch.com>
- [21] Sushko G B, Solov'yov I A and Solov'yov A V 2019 *J. Mol. Graphics Modell.* **88** 247–260
- [22] Ivanov Y M, Petrunin A A and Skorobogatov V V 2005 *Jetp Lett.* **81** 99–101
- [23] Guidi V, Mazzolari A, De Salvador D and Carnera A 2009 *J. Phys. D: Appl. Phys.* **42** 182005
- [24] Camattari R, Guidi V, Bellucci V and Mazzolari A 2015 *J. Appl. Crystallogr.* **48** 977–989
- [25] De Salvador D, Carturan S, Mazzolari A, Bagli E, Bandiera L, Durighello C, Germogli G, Guidi V, Klag P, Lauth W, Maggioni G, Romagnoni M and Sytov A 2018 *J. Instrum.* **13** C04006
- [26] Techno-cls project (ga: 101046458) within the horizon-eic framework URL <https://mbnresearch.com/TECHNO-CLS/Main>
- [27] Korol A V and Solov'yov A V 2020 *Eur. Phys. J.* **74** 201
- [28] Sushko G B, Bezchastnov V G, Solov'yov I A, Korol A V, Greiner W and Solov'yov A V 2013 *J. Comput. Phys.* **252** 404–418
- [29] Molière G 1948 *Z. Naturforsch. A* **3** 78–97
- [30] Fernandez-Pacios L 1993 *J. Comput. Chem.* **14** 410–421
- [31] Taratin A and Vorobiev S 1986 *Phys. Lett. A* **115** 398–400
- [32] Taratin A M and Vorobiev S A 1987 *Phys. Lett. A* **119** 425–428
- [33] Haurylavets V V, Ivanov V K, Korol A V and Solov'yov A V 2024 *Nucl. Instrum. Meth. A* **1058**



168917

- [34] Baier V N, Katkov V M and Strakhovenko V M 1998 *Electromagnetic Processes at High Energies in Oriented Single Crystals* (Singapore: World Scientific)
- [35] Sushko G B, Korol A V, Greiner W and Solov'yov A V 2013 *J. Phys. Conf. Ser.* **438** 012018
- [36] Kaplin V V and Vorobiev S A 1978 *Phys. Lett.* **67A** 135
- [37] Shen H, Zhao Q, Zhang F S, Sushko G B, Korol A V and Solov'yov A V 2018 *Nucl. Instrum. Meth. B* **424** 26
- [38] D J J 1999 *Classical Electrodynamics* (Hoboken: Wiley)
- [39] Tikhomirov V V 2019 *Phys. Rev. Accel. Beams* **22**(5) 054501
- [40] Tikhomirov V V 2020 *Phys. Rev. Accel. Beams* **23**(3) 039901